HHS Public Access

Author manuscript

Acta Biomater. Author manuscript; available in PMC 2019 December 01.

Published in final edited form as:

Acta Biomater. 2018 December ; 82: 34–43. doi:10.1016/j.actbio.2018.10.020.

Effect of working environment and procedural strategies on mechanical performance of bioresorbable vascular scaffolds

Pei-Jiang Wang[#1,2], **Farhad Rikhtegar Nezami**[#1], **Maysam B. Gorji**[3], **Francesca Berti**[1,4], **Lorenza Petrini**[5], **Tomasz Wierzbicki**[3], **Francesco Migliavacca**[4], and **Elazer R. Edelman**[1,6]

[1]Biomedical Engineering Center, Institute for Medical Engineering & Science, Massachusetts Institute of Technology, Cambridge, Massachusetts, 02139, USA

[2]Department of Biomedical Engineering, Boston University, Boston, Massachusetts 02215, USA

[3]Impact and Crashworthiness Laboratory, Department of Mechanical Engineering, Massachusetts Institute of Technology, Cambridge MA, 02139, USA

[4]Laboratory of Biological Structure Mechanics, Department of Chemistry, Materials and Chemical Engineering 'Giulio Natta', Politecnico di Milano, Milano, Italy

[5]Department of Civil and Environmental Engineering, Politecnico di Milano, Milano, Italy.

[6]Cardiovascular Division, Department of Medicine, Brigham and Women's Hospital, Harvard Medical School, Boston, Massachusetts, 02115, USA

[#] These authors contributed equally to this work.

Abstract

Polymeric bioresorbable scaffolds (BRS), at their early stages of invention, were considered as a promising revolution in interventional cardiology. However, they failed dramatically compared to metal stents showing substantially higher incidence of device failure and clinical events, especially thrombosis. One problem is that use of paradigms inherited from metal stents ignores dependency of polymer material properties on working environment and manufacturing/deployment steps. Unlike metals, polymeric material characterization experiments cannot be considered identical under dry and submerged conditions at varying rates of operation.

Maysam B. Gorji: gorji@mit.edu, Farhad Rikhtegar Nezami: farhadr@mit.edu, Francesca Berti: fberti@mit.edu, Lorenza Petrini: lorenza.petrini@polimi.it, Tomasz Wierzbicki: wierz@mit.edu, Francesco Migliavacca: francesco.migliavacca@polimi.it, Elazer R. Edelman: ere@mit.edu. **Corresponding Author:** Pei-Jiang Wang, Room 442, Building E25 at MIT, 45 Carleton St., Cambridge, MA 02142-1323, +17343585085, wpj@mit.edu.

Author Contributions

PJ.W., M.G.B., F.R.N, and E.R.E conceived the ideas and directed the research. PJ.W. and M.G.B. conducted the benchtop tests. PJ.W., M.G.B., and F.B. conducted the FE simulation under guidance of L.P, T.W, and F.M. PJ.W., M.G.B., F.R.N., and F.B. designed the experiments and participated in the analysis and interpretation of the data. PJ.W., M.G.B., F.R.N, F.B. and E.R.E wrote the manuscript. L.P., T.W., and F.M. provided critical revision on the manuscript.

Disclosure

The authors declare that there are no conflict of interests regarding the publication of this article.

We demonstrated different material behaviors associated with variable testing environment and parameters. We, then, have employed extracted material models, which are verified by computational methods, to assess the performance of a full-scale BRS in different working condition and under varying procedural strategies. Our results confirm the accepted notion that slower rate of crimping and inflation can potentially reduce stress concentrations and thus reduce localized damages. However, we reveal that using a universal set of material properties derived from a benchtop experiment conducted regardless of working environment and procedural variability may lead to a significant error in estimation of stress-induced damages and overestimation of benefits procedural updates might offer.

We conclude that, for polymeric devices, microstructural damages and localized loss of structural integrity should complement former macroscopic performance-assessment measures (fracture and recoil). Though, to precisely capture localized stress concentration and microstructural damages, context-related testing environment and clinically-relevant procedural scenarios should be devised in preliminary experiments of polymeric resorbable devices to enhance their efficacy and avoid unpredicted clinical events.

Graphical abstract

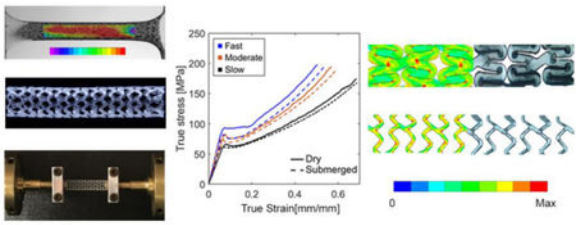

Keywords

Bioresorbable scaffolds; Polymer characterization; Finite element analysis; Working environment; Microstructural damages

1. Introduction

Stent angioplasty has become the golden standard in treating coronary artery diseases mainly because of its minimally-invasive nature and universally-accepted performance scaffolding narrowed vessels, and restoring physiological blood flow. Most state-of-the-art stents currently in the market are made of metal alloys. These permanent foreign objects residing inside living arteries may interfere with vascular repair and lead to various long-term complications [1–7]. Although various approaches have been investigated to improve the performance of these devices [8,9], fundamental limitations associated with metal stents drove the community toward bioresorbable scaffolds (BRS). The emergence of BRS allows implants to be inserted and then degrade over time, leaving an intact vessel.

Poly-l-lactic acid (pLLA) is currently the most commonly used material for BRS. However, it is fundamentally different from metals, in terms of its dynamic properties, material behavior, and heterogeneous microstructures [10]. These unique features require distinct

research paradigms that cannot be assumed to mimic metal devices. When we update our stent material from durable metals to degradable polymers, and expect they perform the same way, we must also update the way we characterize and evaluate the material properties and the devices with respect to working environment. Updated preliminary tests, respecting material characteristics of the device and working environment, will lead to design of a new generation of devices with an enhanced clinical performance. Ignoring such differences and simply inheriting evaluation strategies from other durable materials might well bring catastrophic clinical outcomes, and may be, in part, why mounting clinical evidences show increased rate of thrombosis and myocardial infarctions with BRS [11,12].

Coronary stents undergo a 2- to 3-fold radial reduction at crimping and equal or more expansion at implantation, and are exposed to cyclical asymmetric strain from each heartbeat. Rigorous benchtop experiments are thus enforced to provide thorough mechanical characterizations on these devices [13–15]. In addition, the irregular and complex structural design of stents relies increasingly on finite element (FE) analysis drawing on material mechanical responses characterized from benchtop stress-strain tests [16–19]. Yet, the accuracy of FE analysis highly depends on benchtop mechanical characterization.

Unlike metals which possess relatively-stable mechanical properties under physiological conditions, mechanical responses of polymer materials, such as pLLA, vary largely due to their high sensitivity in testing environment. We hereby emphasize that material behavior would critically change depending on the operation environment. The fact that BRS are designed and tested in dry test room condition, and then implanted in continuous contact to blood flow may cast serious doubt on the accuracy of preliminary design steps when material characterization might not comply with realistic material behavior in situ. Differences in yield strain, stiffness, strain at break and ultimate tensile strength have been found when tested in air and in submerged conditions [13] while majority of studies relied on one condition ignoring the implications of the other in terms of more comprehensive material characterization. Furthermore, limited studies have appreciated this critical concept, specifically while modeling the device performance and treatment efficacy. According to the operation environment of BRS, as the crimping is done in air while the inflation is performed when BRS is inserted into the artery and in contact with blood, the design analysis and structural modeling should accordingly consider material properties tested under both scenarios instead of a single universal model for all.

In addition to distinguishing the environment the device is exposed to, the rate of crimping and inflation may also alter its mechanical properties due to viscosity [17]. There has been a strict implantation instruction devised by BRS manufacturers for physicians to follow in terms of designated deployment rate, substantially slower compared to metal stents, to prevent acute fractures or reduce recoil during/after implantation [20]. Yet, no explicit limit has been set to specify the optimal rate. One important circumstance that has also been ignored thus far is the fact that crimping, as well, creates microstructural deformations which may develop into more severe structural failures in future [10]. Proper investigation of crimping and inflation rate is required to minimize microstructural failures and ensure optimal practice in clinics. This fundamental aspect of BRS design has been the central scope of this research, then, to characterize the device in acute time frame with respect to the

environment and later assess their performance in the context of intervention. We conducted uniaxial tensile tests on dog-bone samples obtained through laser cutting clinical-grade pLLA tubes. Tests were performed in both air and submerged conditions at different velocities. FE analysis was then performed with material properties derived from both conditions to help compare stress distribution and recoil percentage (%recoil) to verify the efficacy of device. This extensive approach of material characterization and device performance assessment may shed further light on the mechanistic knowledge of how the BRS would behave at their early stages of service in physiological settings to not only delineate a portion of clinical events observed for BRS but also provide design teams with insights to upgrade medical devices for enhanced clinical treatments.

2. Material and Methods

2.1 Material Preparation

pLLA (molecular weight ~ 600K g/mol, inherent viscosity ~6.7 dl/g, Changchun SinoBiomaterials Co., Ltd., China) dog-bone specimens and fully-resorbable pLLA scaffold systems provided by the Boston Scientific Corporation were used in all experimental conditions unless otherwise specified. All units tested were prototypes under development and not commercially available. Scaffolds are 16 mm in length, 3.0 mm in inner diameter before crimping, and have a wall thickness of 105 μm (Figure 1A). Dog-bone specimens were obtained through laser-cutting using the same extruded tubes used to generate scaffolds (Figure 1B), and then flattened with weights prior to experiments. All specimens were carefully extracted having the loading axis aligned with the longitudinal axis of the extruded PLLA tube. Scaffolds and dog-bone specimens were stored at 4 °C prior to experiments.

2.2 Uniaxial tensile test on pLLA dog bone specimens

Mechanical properties of the material were predominantly characterized by the uniaxial tensile test. The hardening curve resulted from the experiment describing evolution of the yield stress during the deformation. In a real-world working environment, scaffolds are in direct contact with blood once being inserted into a patient’s artery. It normally takes clinicians a few minutes to reach the target lesion site and inflate the balloon. Thus, to better mimic the real clinical practices, the experimental setup (Figure 1C, Bangalore Integrated System Solutions, India) included a water chamber to allow the specimens stretching after 10 minutes of immersion. In this manner we isolate the effects of mechanical forces and immersion on device performance including degradation long before hydrolysis and classic erosive forces emerge. A dog-bone specimen was mounted onto two clamps, immersed in water for 10 minutes at room temperature, and then stretched by the presented testing machine. The axial load cell signals were recorded in real-time and compiled by a computer-based data acquisition system. Experiments were accomplished in the range of quasi-static to dynamic stretching condition with three constant cross-head velocities, 0.001, 0.01, and 0.1 mm/sec, defined as slow, moderate and fast, correspondingly, until fracture. It is safe to assume the slowest velocity, 0.001 mm/sec, as a quasi-static condition. Four specimens were tested in each of the fast and moderate scenarios.

Deformations were observed and recorded by the Digital Image Correlation (DIC) method. This non-contact and material-independent optical measuring system is extensively being used to monitor the displacement history and strain distribution in mechanical applications [21, 22]. All experiments – in dry and submerged conditions – were monitored with a high resolution digital camera. Front surfaces of all specimens were speckle-painted using an airbrush leaving behind randomly patterned black points. The resulted images including the entire experiment up to fracture were then imported to the DIC software, VIC-2D (Correlated Solutions), to quantify the displacement field and the planar surface strains. Effective strain distribution of uniaxial tensile samples subjected to different stretching velocities before fracture were assessed for both dry and submerged conditions (Figure 2).

2.3 Material Parameters Calibration

Material parameters for the numerical analysis were extracted from the true stress – true strain experimental curves. The Young's modulus was calculated based on the elastic region of the experiment. Abaqus/Standard 2017 (Dassault Systèmes, Providence, RI, USA) was used as finite element software. Johnson-Cook plasticity model was employed to capture the non-linear material hardening behavior after yielding and the strong dependency on testing velocities. The temperature dependence of the model was deactivated as the tests were conducted under the glass transition temperature $\bar{\sigma}$ is reported hereinafter:

$$\bar{\sigma} = \left[C_1 + C_2(\bar{\varepsilon}^{pl})^n\right][1 + C_3 \ln(\dot{\bar{\varepsilon}}^{pl}/\dot{\bar{\varepsilon}}^0)]$$

where $\bar{\varepsilon}^{pl}$ is the equivalent plastic strain, C_1, C_2, C_3, n, and $\dot{\bar{\varepsilon}}^0$ are material parameters of the model and $\dot{\bar{\varepsilon}}^{pl}$ is the equivalent plastic strain rate. C_1 is the yield stress in static conditions, which is assumed to be the value at the "slow" velocity. C_2 and n regulate the shape of the static curve in terms of the slope and concavity. C_3 is the scaling parameter between the static material curve and the response at different strain rates. The parameters for both dry and submerged scenarios were identified by enforcing the exact match of the analytically-calculated curves over the experimental ones obtained at three different velocities. In addition, a symmetric behavior in tension and compression are assumed in the model.

2.4 Verification of Material Properties

A dog-bone-shaped 3D model was implemented in Abaqus/Standard to numerically replicate the experimental uniaxial tensile tests, wherein all dimensions and parameters accurately traced the experimental settings. A dynamic/implicit solver was used to simulate all six scenarios with parameters identified above. Displacements in all directions were constrained ($U_X = U_Y = U_Z = 0$) on one end of the specimen while a uniaxial displacement ($U_X \neq 0$) was applied in a fixed time span (ΔT) on the other, duplicating the experiment. The model was discretized by means of 8-node linear brick reduced integration elements (C3D8R). A sensitivity analysis on the refinement was conducted up to an element size of about 0.05 mm. The applied displacement and the reaction force were extracted and compared in a forcedisplacement plot to the experimental counterparts (Table I)

2.5 3D Validation by scaffold geometry

A longitudinal tensile and a lateral crush resistance test were conducted on real scaffolds to validate the robustness of both the material and geometrical numerical descriptions. Both tests were conducted in a setting more akin to clinics, i.e. submerged environment under displacement control, and moderate velocity. In the longitudinal tensile test, scaffolds were fixed onto a tensile tester (Figure 3A) and stretched at a constant velocity of 0.1 mm/sec for 70 seconds. In the lateral crush resistance test, scaffolds were placed in the middle of two flat plates (Figure 3C) and compressed at a constant velocity of 0.1 mm/s up to a displacement of 2 mm. These conventional tests were chosen due to their simplicity and similarity to invivo loads experienced by BRS.

A 3D finite element model of the scaffold was constructed in Abaqus/Implicit to validate the material model (Figure 3B&D). The mesh of 8-node linear brick, incompatible mode element (C3D8I) was created by Hypermesh (Altair Hyperworks). Incompatible modes elements were chosen based on their accepted performances in describing bending-dominated problems such as the one occurring in scaffold deformation during crimping and inflation. The total number of elements is 242’785, with four elements designated across the strut thickness.

The numerical models were implemented in a dynamic/Implicit simulation, exactly replicating the geometries, applied boundary conditions, and duration of the experiments. Material properties derived from submerged conditions were used in this analysis since experiments were conducted in water. The elastic modulus was set to 1.4 GPa. In the longitudinal tensile test (Figure 3B), both ends of the scaffold were linked to two multipoint constraints (MPCs); one end was fixed ($U_X = U_Y = U_Z = UR_1 = UR_2 = UR_3 = 0$) while the other was under axial tension ($U_Z = 7$ mm). The total step time was set to 74 seconds in chorus to the experiment. In the lateral crush resistance test (Figure 3D), an unconstrained scaffold was positioned between two identical planar rigid surfaces (quadrilateral surface element with reduced integration, SFM3D4R, 341 elements). The bottom surface was constrained as fixed ($U_X = U_Y = U_Z = UR_1 = UR_2 = UR_3 = 0$) while the top surface vertically moved ($U_Y = 2$ mm), impacting the lateral surface of the scaffold with compression forces. The contact was defined as “hard contact” with the friction coefficient of 0.2 between the surfaces and the scaffold. The total step time was set to 20 seconds according to the experiment. In both cases, the applied displacement and the reaction force were extracted and compared in a force-displacement plot to the experimental counterparts.

2.6 FE analysis of scaffold crimping and inflation

Employing Abaqus/Explicit, crimping and inflation were solved incorporating two sets of material properties, dry and submerged, for a scaffold with the same geometrical design as in previous experiments. The simulation set-up strived to mimic a real clinical intervention scenario. The time-scaling factor has been set to 1 with a target time increment of 1×10^{-4}. Interaction between all the surfaces was defined as “general contact” with a friction coefficient of 0.2. The framework of the simulation and its steps could be described as follow:

1. *Crimping*: An unconstrained scaffold (density = 1.4 g/cm^3) was radially compressed by an external rigid cylindrical surface (initial diameter of 3.2 mm, quadrilateral surface element with reduced integration, SFM3D4R, 3'952 elements). A radial displacement of 1 mm was applied to all nodes;
2. *Release*: The rigid surface was removed to let the scaffold recoil freely; Step time was set to 10 sec.
3. *Intraluminal positioning*: The crimped scaffold was positioned inside the lumen of a mock vessel. The model consisted of a linear elastic cylinder (density = 1.16 g/cm^3, E = 1.46 MPa, Poisson's ratio = 0.3, internal lumen diameter = 3.0 mm, thickness = 0.5 mm) made of 100'500 8-node linear brick, incompatible modes elements (C3D8I).
4. *Inflation*: An internal cylinder (initial diameter = 1.0 mm, with 1'400 quadrilateral surface elements with reduced integration, SFM3D4R) radially expanded the scaffold to the final inner diameter of 3.4 mm (about 12% of overexpansion to guarantee the perfect apposition at the end of the procedure).
5. *Relaxation*: The internal cylinder was maintained at the expanded state with the step time of 30 sec to allow stress relaxation in the scaffold.
6. *Recoil*: The internal cylinder was reduced to 0.1 mm to allow the scaffold recoil freely.

Three different step times were considered for crimping and inflation (step 1 and 4) to evaluate the effect of operation rate on the scaffold performance (Table II).

Values of the von Mises equivalent stress (MISES) were extracted at the end of the crimping and inflation phases to assess the effect of operation procedural rate on stress concentration. Recoiling percentage (%Recoil) was also calculated for all scenarios using:

$$\%Recoil = \left(D_1 - D_2\right)/D_1$$

where D_1 and D_2 are the outer diameter of the scaffold at the end inflation and recoil steps, respectively.

3. Result

3.1 Mechanical Response of pLLA

True stress – true strain curves were plotted to compare dry and submerged samples at three different testing velocities including 0.1 mm/s, 0.01 mm/s, and 0.001 mm/s (Figure 4). Similar visco-plastic behavior was observed for all loading conditions, i.e. after passing the yield point, a small amount of stress softening was followed by stress hardening till the sample fractured. The minimum stress evolution was recorded under the quasi-static condition in both dry and submerged conditions. In dry condition (solid lines), lower velocity leads to lower elastic modulus (E), higher yield strain $\left(\bar{\varepsilon}_y\right)$, lower yield stress $\left(\bar{\sigma}_y\right)$, higher fracture strain $\left(\bar{\varepsilon}_f\right)$, and higher fracture stress $\left(\bar{\sigma}_f\right)$ (Table III). In submerged condition

(dash lines), the effect of testing velocity on mechanical responses are not as clear as in dry cases. Although $\bar{\varepsilon}_f$, $\bar{\sigma}_y$, and $\bar{\sigma}_f$ in submerged condition have similar trends as in dry condition, the fast and moderate samples show comparable elasticity, which reduces when experiment velocity is the slowest. At a comparable velocity, a clear difference can be seen between dry and submerged conditions, wherein reducing the testing velocity diminishes the observed disparities. This observation emphasizes the necessity to apply proper mechanical properties during FE analysis. In general, submerged samples exhibit less resistance to yielding, higher deformability, and softer behavior compared to dry cases. Two-tailed, unequal variance Student t test were performed and a P value <0.05 was considered to denote statistical significance. Yield strain is significantly lower in submerged condition in both fast and moderate scenarios ($p = 0.017$ and 0.031 in fast and moderate scenarios, respectively). In addition, yield stress is also significantly lower in submerged condition in moderate scenarios ($p = 0.028$).

3.2 Verification by the FE model

True stress – true strain curves generated from FE analysis mimicking a uniaxial tensile test on dog-bone specimens were highly correlated to results obtained from benchtop tests in both dry and submerged conditions (Table IV, Figure 5A and5B). In addition, experimental force – displacement curves for full-scale scaffold tests, including the longitudinal tensile test and the lateral crush resistance test, were dependably followed by FE results using the same set of parameters (Figure 5C and 5D).

3.3 Scaffold performance in procedural scenarios

Stresses concentration was highly correlated to specific design features which caused localized deformations (Figure 6). More specifically, after crimping, deformations were clearly visible in experiments and predicted by the numerical simulation at inner peak edges (Figure 6A). However, device inflation promoted deformations at outer peak edges (Figure 6B), wherein development of inner sides' deformations into micro-cracks were observed (Figure 6C). These alterations in structural integrity prior and during scaffold implantation may potentially develop into catastrophic structural failures after implantation in situ and may, in part, explain events observed in clinical trials.

As a representative measure of regions with the risk of failure, the percentage of elements with von Mises stresses higher than 50% and 75% of the ultimate stress ($0.5\times\sigma_u$, $0.75\times\sigma_u$) were quantified after scaffolds and 9% of elements experienced stresses higher than 0.5× , respectively at fast, moderate, and slow rates. (Figure 7A). While in submerged samples, lower percentage of elements experienced the same level of high stresses at similar crimping rates, i.e. 11%, 11%, and 10% when crimped at fast, moderate and slow rate, respectively (Figure 7B). Inflation of the device exerts critical stresses to a higher number of device elements in both dry and submerged conditions (Figure 7C and D). Comparing the submerged and dry samples, reducing the rate of crimping and/or inflation considerably drops the percentage of elements experiencing high stresses in the latter. In general, low, yet concerning proportion of elements experience stresses beyond the fracture point, with higher values for dry samples. In addition, in both working environments, %recoil were within the range of 8 to 10, which is in accordance with what has been reported in clinics for this

viscoelastic-plastic device. Overall, the percentage of elements experiencing extreme levels of stresses decreases as the operation slows down regardless of the environment the specimen is exposed to. Slow operational rate may potentially reduce stress concentration, and thus lower potential damages caused by deformations.

4. Discussion

Stents experience extreme stresses and large deformations while being crimped or inflated, which is even before they serve scaffolding diseased vessels under cyclic asymmetric loadings. These loads may increase the likelihood of mechanical failure for BRS even more than their metallic counterparts - not just because the latter are stronger but also because the stress-strain response of the two materials is fundamentally different. Moreover, unlike metals, polymeric materials are far more sensitive to changes in environmental (immersive vs dry, warm vs hot contexts etc.). Tests that are standard for metal devices might therefore not be appropriate for polymeric constructs. Simply inheriting design paradigms of metal stents to develop BRS, in which the environment and procedural effects on device performances have often been ignored, might lead to incorrect assessment of mechanical stressors the device faces. Most studies have relied on employing a single set of material properties derived from benchtop experiments, usually uniaxial tensile tests, conducted under one testing environment, i.e. in air or in a submerged environment, to feed higher-level analyses of device performance, e.g. crimping, inflation, and load bearing capability [13,23]. However, viscoelastic-plastic polymers, such as pLLA, consist of heterogeneous microstructural compartments including crystal domains, where molecules are differentially aligned and packed, and amorphous regions where they are randomly oriented. Macroscopic properties of such materials, e.g. mechanical strength, deformability, yield resistance, and degradation greatly depend on their microscopic characteristics such as molecular orientation and degree of crystallinity [24]. This dependency leads to completely different mechanical responses when tested in diverse environments, e.g. in a submerged condition akin to vessel lumen, with lower yielding resistance, higher deformability, and softer behaviors (Figure 4 and 5). Observed differences between dry and submerged condition may be due to the alterations in crystallinity and molecular orientation caused by re-crystallization and swelling as materials absorb water molecules [10,25]. We suspect that water molecules within the polymeric matrix act as a resisting buffer damping the deforming forces and alleviating the effect of procedural rates.

The dependency of material properties on the working environment is, thus, important considering the varying environment BRS are exposed to. In practice, BRS crimping is usually performed, as a step in the manufacturing possess, in air with 37 °C or higher degrees to reduce material stiffness and prevent microcracks. Whereas, BRS inflation is routinely performed in clinics within 10 minutes after balloon-mounted devices are inserted in a submerged environment at body temperature. Such significant disparities in the operation environment mandate engineers and designer to conduct device characterization in corresponding realistic scenarios, and if ignored may lead to unreliable regulatory tests and eventually unpredictable clinical behaviors. Lack of thorough understanding of BRS mechanical behavior might well have contributed to the inability to foresee clinical consequences [9, 26–28].

Intriguingly, corrective strategies to reduce clinical failures have focused more on refining implantation techniques and vessel preparation than in understanding material dynamics [20]. Clinicians have been advised to adhere to a strict implantation protocol that includes lesion pre-dilation and controlled inflation of these devices at a much slower rate compared to their metallic counterparts to prevent acute fracture, and reduce recoil [20]. However, not only there is no clear-cut measure on what the optimal rate should be, but also proper criteria specifically designed for BRS to determine optimal rate are still missing. Criteria inherited from metal stent guidelines which mainly focus on preventing acute fracture, and reducing recoil may not be comprehensive enough. The implication of our work is that designers should conduct updated preliminary tests, more related to the device-specific material properties and working environment, to achieve a comprehensive understanding and predictive measure of performance for these novel devices.

Due to the differences in mechanical behavior when being characterized in dry and submerged conditions (Figure 4), different levels of stress concentration have been noticed with FE analysis on crimping and inflation of resorbable devices. Crimping the scaffold at a slower rate could potentially reduce the risk of exposing large percentage of elements to high stresses (Figure 7A). This benefit can easily be overlooked when we simulate crimping with material models derived from a test under the submerged condition (Figure 7B). In addition, a higher percentage of elements underwent high stresses in dry conditions compared to submerged conditions (specifically in fast velocities), which raises the concern that one may underestimate the severity of stress concentration during the crimping and miss potential modes of failure. Similarly, if an inflation model is supported by a material predicted performance derived from dry sample characterization, the procedural effect of inflation time on reducing stress concentration could be noticeably overestimated. Reducing inflation time from 10 to 40 seconds (fast to slow) can reduce the number of elements experiencing high stresses by 22% and 7% in indicated high risk categories ($0.5\times\sigma_u$ and $0.75\times\sigma_u$, respectively) in dry condition (Figure 7C), but only 3% and 1% when submerged (Figure 7D). Slow inflation then can potentially reduce the relative number of elements exposed to high stresses. However, minimization of device failure solely by further reduction of inflation rate (to a rate far beyond the routine practices of BRS) might not be sufficient if the submerged rather than dry conditions dictate the range of change that can be achieved. We might therefore reconsider the idea that one model alone can provide a comprehensive understanding and accurate prediction on the device performances.

Percentage of recoil and acute macro-structural fractures are the two most commonly used criteria when assessing the performance of implanted device. However, noticed in our FE analysis, inflating at slower rate seems to have very limited effect on preventing recoil (2% difference in %recoil between fast and slow scenarios), as long as clinicians follow the instruction of holding the scaffold at the end of inflation for at least 30 sec. Thus, procedural factors might alleviate/exacerbate structural responses and consequently alter the performance measures such as recoil due to their direct influence on material properties. However, the material behavior change, as a result of interventional procedure alteration, is extremely nonlinear. Corrective strategies merely focused on procedural parameters without noticing their complex effect on material modulation may, thus, be misleading as they rely on performance measures inherited from metallic counterparts. In addition, several *in vitro*

and *in vivo* experiments have shown that acute fractures could be avoided when slow inflation is warranted. Yet, the catastrophic clinical events linger in clinical trials with a higher failure rate compared to metal stents during acute time settings. As a result, continuing to use %recoil and acute macro-structural fracture as mere criteria to assess the device efficacy may be no longer a reliable approach nor an accurate prediction tool for future research in BRS evolution.

Instead, we hypothesize that it might be the microstructural composition of such a heterogeneous material, its evolution over the rigorous interventional procedure, and acute/long-term exposure to dynamic biological environment within the body that determine the device performance. Complete understanding of the function of devices with dynamic material properties can be considered as the coordinated, interdependent, and integrated sum over time of mechanical stresses, operating environment, material heterogeneities, and erosive forces. Heterogeneities in BRS material properties induce microstructural damages at certain design features (Figure 6) during manufacturing/clinical routines. These localized microscopic damages challenge the structural integrity of the devices at an early stage, and as they further experience the complex biological and mechanical environment in situ, fatigue-induced crack propagation, and strain-induced degradation may happen at an unexpected accelerated rate and potentially develop into catastrophic failures in macro-structures, such as malapposition, large recoil, and fracture leading to reported clinical events [10,29]. Performing the present work, we have more focused on acute time-frame of BRS performance and further highlighted the importance of incorporating micro-structural damages such as localized deformation and micro-cracks as device evaluation criteria. Updates on procedural strategies (reducing inflation or crimping rate for instance) may successfully reduce the risk of microstructural damages (reducing the stress concentration in certain spatial locations). However, ignoring the effect of environment in which the device operates on material characteristics, and consequently on preliminary simulations of design and development, may result in exaggeration of this benefit.

This study bears a number of limitations that are aimed to be improved in the future. Since mechanical behaviors of polymeric material such as pLLA largely depend on its molecular structure, mechanical tests could be more comprehensive if uniaxial tests were conducted on samples cut along both axial and circumferential directions of the extruded tubes to include anisotropic behaviors. As part of the scaffold undergoes significant compression during crimping and inflation process, more accurate FE analysis would entail conducting a compression test to ensure the validity of symmetric behavior assumption in tension/compression, especially for post yield behavior. In addition, validation of the model in all modes of operation, i.e. slow, moderate, and fast, and different working environment, i.e. dry and submerged, is encouraged to further ensure the robustness of the model on intact device performances.

5. Conclusion

Multiple instances of failure reported for the first generation BRS has warranted the necessity of closing the gap between preliminary benchtop predictions and clinical observations. Research paradigms inherited from metal stents should not be applied to BRS

due to their substantial differences in material characteristics, which may mislead designers to seek problem sources at erroneous timeframes. Accurate material models warrant realistic inputs into, and thus reliable outcome out of, high-level design analyses of crimping, inflation, and load bearing capability. This entails including the effect of working environment and procedural strategies on mechanical responses to enhance mechanistic understanding of material behaviors of BRS and predict potential clinical failures. Applying a universal set of material properties to study the device performance in different phases of manufacturing/implantation may result in inaccurate assessment of stress concentration and unpredictable device failure. Similarly, for polymeric devices, microstructural damage might be a more superior criterion to assess structural integrity and device efficacy rather than previously-perceived acute fractures and recoil percentage.

Acknowledgements

The authors gratefully thank Boston Scientific Corporation (Marlborough, MA) for partial grant support and generous supply of test specimens and scaffolds. ERE and FRN are supported in part by R01 from National Institutes of Health (R01 GM 49039). F.B. and F.M. were partially supported by the Fondazione Fratelli Agostino and Enrico Rocca through a Progetto Rocca doctoral fellowship. The authors would also like to thank our reviewers for improving the quality of this work with their valuable suggestions.

Reference:

[1]. Lee MS, Jurewitz D, Aragon J, Forrester J, Makkar RR, Kar S, Stent fracture associated with drug-eluting stents: clinical characteristics and implications, Catheter. Cardiovasc. Interv 69 (2007) 387–94. [PubMed: 17195203]

[2]. Lee SH, Park JS, Shin DG, Kim YJ, Hong GR, Kim W, Shim BS, Frequency of Stent Fracture as a Cause of Coronary Restenosis After Sirolimus-Eluting Stent Implantation, Am. J. Cardiol 100 (2007) 627–630. [PubMed: 17697818]

[3]. Kolandaivelu K, Rikhtegar F, The Systems Biocompatibility of Coronary Stenting, Interv. Cardiol. Clin 5 (2016) 295–306. [PubMed: 28582028]

[4]. Edelman ER, Wang PJ, Needles in Our Technology Haystacks: Defining Efficacy Is Easy, Characterizing Complications Is the Challenge, Circulation: Cardiovasc. Interv 10 (2017) e006059

[5]. Spaulding C, Daemen J, Boersma E, Cutlip DE, Serruys PW, A Pooled Analysis of Data Comparing Sirolimus-Eluting Stents with Bare-Metal Stents, N. Engl. J. Med 356 (2007) 989–997. [PubMed: 17296825]

[6]. Stettler C, Wandel S, Allemann S, Kastrati A, Morice MC, Schömig A, Pfisterer ME, Stone GW, Leon MB, de Lezo JS, Goy JJ, Park SJ, Sabaté M, Suttorp MJ, Kelbaek H, Spaulding C, Menichelli M, Vermeersch P, Dirksen MT, Cervinka P, Petronio AS, Nordmann AJ, Diem P, Meier B, Zwahlen M, Reichenbach S, Trelle S, Windecker S, Jüni P, Outcomes associated with drug-eluting and bare-metal stents: a collaborative network meta-analysis, Lancet 370 (2007) 937–948. [PubMed: 17869634]

[7]. Stone GW, Moses JW, Ellis SG, Schofer J, Dawkins KD, Morice MC, Colombo A, Schampaert E, Grube E, Kirtane AJ, Cutlip DE, Fahy M, Pocock SJ, Mehran R, Leon MB, Safety and Efficacy of Sirolimus- and Paclitaxel-Eluting Coronary Stents, N. Engl. J. Med 356 (2007) 998–1008. [PubMed: 17296824]

[8]. Adamo RF, Fishbein I, Zhang K, Wen J, Levy RJ, Alferiev IS, Chorny M, Magnetically enhanced cell delivery for accelerating recovery of the endothelium in injured arteries, J. Control. Release 222 (2016) 169–175. [PubMed: 26704936]

[9]. Jiménez JM, Prasad V, Yu MD, Kampmeyer CP, Kaakour AH, Wang PJ, Maloney SF, Wright N, Johnston I, Jiang YZ, Davies PF, Macro- and microscale variables regulate stent haemodynamics, fibrin deposition and thrombomodulin expression., J. R. Soc. Interface 11 (2014) 20131079. [PubMed: 24554575]

[10]. Wang PJ, Ferralis N, Conway C, Grossman JC, Edelman ER, Strain-induced accelerated asymmetric spatial degradation of polymeric vascular scaffolds, Proc. Natl. Acad. Sci. U. S. A 2018.

[11]. Collet C, Asano T, Sotomi Y, Cavalcante R, Miyazaki Y, Zeng Y, Tummala K, Stanetic B, Tijssen J, DE Winter R, Onuma Y, Capodanno D, Serruys PW, Early, late and very late incidence of bioresorbable scaffold thrombosis: a systematic review and meta-analysis of randomized clinical trials and observational studies, Minerva Cardioangiol 65 (2017) 32–51. [PubMed: 27626924]

[12]. Tanaka A, Latib A, Kawamoto H, Jabbour R, Sato K, Miyazaki T, Naganuma T, Mangieri A, Pagnesi M, Montalto C, Chieffo A, Carlino M, Montorfano M, Colombo A, Clinical outcomes of a real-world cohort following bioresorbable vascular scaffold implantation utilising an optimised implantation strategy, EuroIntervention, 12 (2017) 1730–1737. [PubMed: 27746400]

[13]. Pauck RG, Reddy BD, Medical Engineering & Physics Computational analysis of the radial mechanical performance of PLLA coronary artery stents, Med. Eng. Phys 37 (2015) 7–12. [PubMed: 25456397]

[14]. Dreher ML, Nagaraja S, Batchelor B, Effects of fatigue on the chemical and mechanical degradation of model stent sub-units, J. Mech. Behav. Biomed. Mater 59 (2016) 139–45. [PubMed: 26759973]

[15]. Barragan P, Garitey V, Mouneimne K, Rieu R, Longitudinal compression behavior of coronary stents: a bench-top comparative study, EuroIntervention, 9 (2014) 1454–1462. [PubMed: 24755385]

[16]. Bobel AC, Petisco S, Sarasua JR, Wang W, McHugh PE, Computational Bench Testing to Evaluate the Short-Term Mechanical Performance of a Polymeric Stent, Cardiovasc. Eng. Technol 6 (2015) 519–532. [PubMed: 26577483]

[17]. Bobel AC, Lohfeld S, Shirazi RN, McHugh PE, Experimental mechanical testing of Poly (L-Lactide) (PLLA) to facilitate pre-degradation characteristics for application in cardiovascular stenting, Polym. Test 54 (2016) 150–158.

[18]. Grogan JA, Leen SB, Mchugh PE, Biomaterials Optimizing the design of a bioabsorbable metal stent using computer simulation methods, Biomaterials, 34 (2013) 8049–8060. [PubMed: 23906516]

[19]. Naseem R, Zhao L, Liu Y, Silberschmidt VV, Experimental and computational studies of poly-L-lactic acid for cardiovascular applications: recent progress, Mech. Adv. Mater. Mod. Process 3 (2017) 13.

[20]. Ortega-Paz L, Capodanno D, Gori T, Nef H, Latib A, Caramanno G, Di Mario C, Naber C, Lesiak M, Capranzano P, Wiebe J, Mehilli J, Araszkiewicz A, Pyxaras S, Mattesini A, Geraci S, Naganuma T, Colombo A, Munzel T, Sabaté M, Tamburino C, Brugaletta S, Predilation, sizing and post-dilation scoring in patients undergoing everolimus-eluting bioresorbable scaffold implantation for prediction of cardiac adverse events: development and internal validation of the PSP score, EuroIntervention, 12 (2017) 2110–2117. [PubMed: 28246060]

[21]. Gorji MB, Mohr D, Micro-tension and micro-shear experiments to characterize stress-state dependent ductile fracture, Acta Materialia, 131 (2017) 65–76

[22]. Gorji MB, Tancogne-Dejean T, Mohr D, Heterogeneous random medium plasticity and fracture model of additively-manufactured Ti-6Al-4V, Acta Materialia, 148 (2018) 442–455

[23]. Wang Q, Fang G, Zhao Y, Wang G, Cai T, Computational and experiment investigation into mechanical performances of Poly-L-Lactide Acid (PLLA) coronary stents, J. Mech. Behav. Biomed. Mater 65 (2017) 415–427. [PubMed: 27643678]

[24]. Han X, Pan J, A model for simultaneous crystallisation and biodegradation of biodegradable polymers, Biomaterials 30 (2009) 423–430. [PubMed: 18952280]

[25]. Agrawal CM, Hass KF, Leopold DA, Clark HG, Evaluation of poly(L-lactic acid) as a material for intravascular polymeric stents, Biomaterials, 13 (1992) 176–182. [PubMed: 1567942]

[26]. Lipinski MJ, Escarcega RO, Baker NC, Benn HA, Gaglia MA, Torguson R, Waksman R, Scaffold Thrombosis After Percutaneous Coronary Intervention with ABSORB Bioresorbable Vascular Scaffold, JACC Cardiovasc. Interv 9 (2016) 12–24. [PubMed: 26762906]

[27]. Serruys PW, Chevalier B, Sotomi Y, Cequier A, Carrié D, Piek JJ, Van Boven AJ, Dominici M, Dudek D, McClean D, Helqvist S, Haude M, Reith S, de Sousa Almeida M, Campo G, Iñiguez

A, Sabaté M, Windecker S, Onuma Y, Comparison of an everolimus-eluting bioresorbable scaff old with an everolimus-eluting metallic stent for the treatment of coronary artery stenosis (ABSORB II): a 3 year, randomised, controlled, single-blind, multicentre clinical trial, Lancet 388 (2016) 2479–2491. [PubMed: 27806897]

[28]. Kolandaivelu K, Swaminathan R, Gibson WJ, Kolachalama VB, Nguyen-Ehrenreich KL, Giddings VL, Coleman L, Wong GK, Edelman ER, Stent Thrombogenicity Early in High-Risk Interventional Settings Is Driven by Stent Design and Deployment and Protected by Polymer-Drug Coatings, Circulation, 123 (2011) 1400–1409. [PubMed: 21422389]

[29]. Sotomi Y, Suwannasom P, Serruys PW, Onuma Y, Possible mechanical causes of scaffold thrombosis: insights from case reports with intracoronary imaging, EuroIntervention, 12 (2017) 1747–1756. [PubMed: 27773862]

Statement of Significance

Bioresorbable scaffolds (BRS) with the hope to become the next cardiovascular interventional revolution failed in comparison to metal stents. When BRS were characterized using methods for metal stents, designers were misled to seek problem sources at erroneous timeframe and use inefficient indicators, and thus no signal of concern emerged. We demonstrated fundamental flaws associated with applying a universal set of material properties to study device performances in different phases of manufacturing/implantation, and these may be responsible for failure in predicting performance in first-generation BRS. We introduced new criterion for the assessment of structural integrity and device efficacy in next-generation BRS, and indeed all devices using polymeric materials which evolve with the environment they reside in.

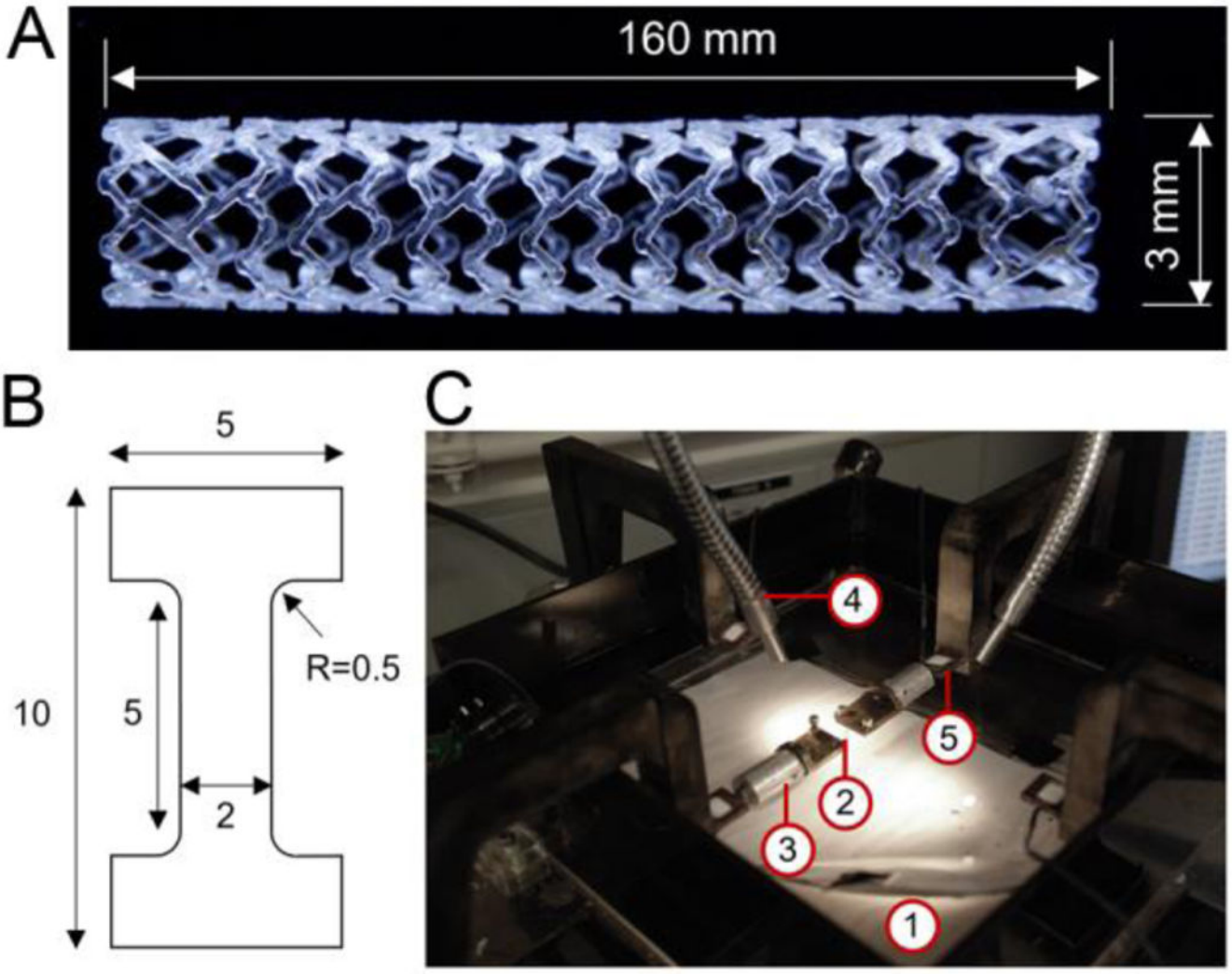

Fig. 1.

Scaffold and experimental setup for uniaxial test on dog-bone specimen. (A) Bioresorbable scaffold. (B) Dog-bone specimen dimensions in mm. (C) Biaxial tensile tester with (1) water chamber; (2) dog-bone specimens; (3) clamps; (4) solid-state semiconductor LED lightening; and (5) load cell.

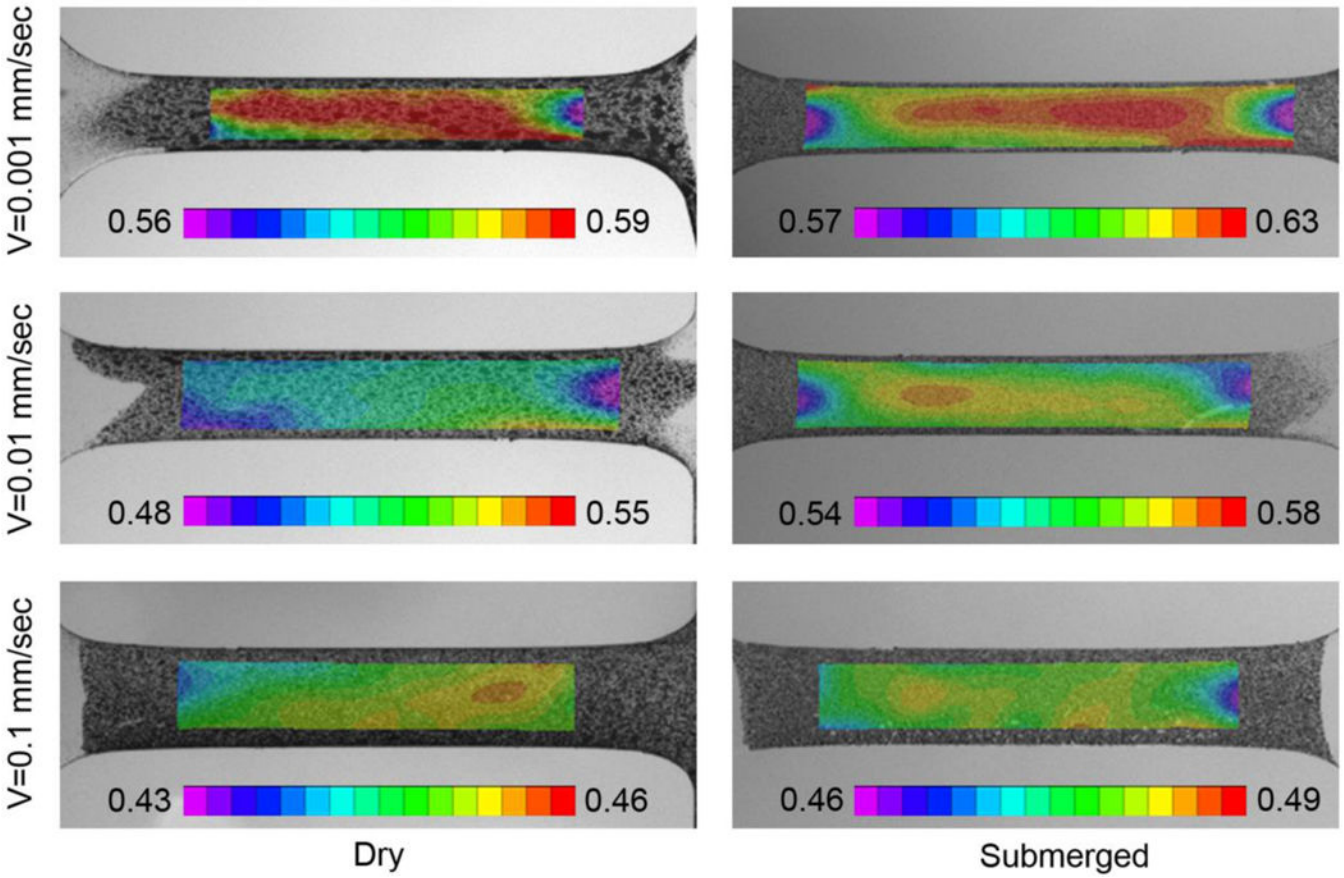

Fig. 2.

Effective strain distribution of uniaxial tensile samples for dry and wet conditions subjected to different stretching velocities. Colored scale bar indicates strain. (For interpretation of the references to color in this figure legend, the reader is referred to the web version of this article.)

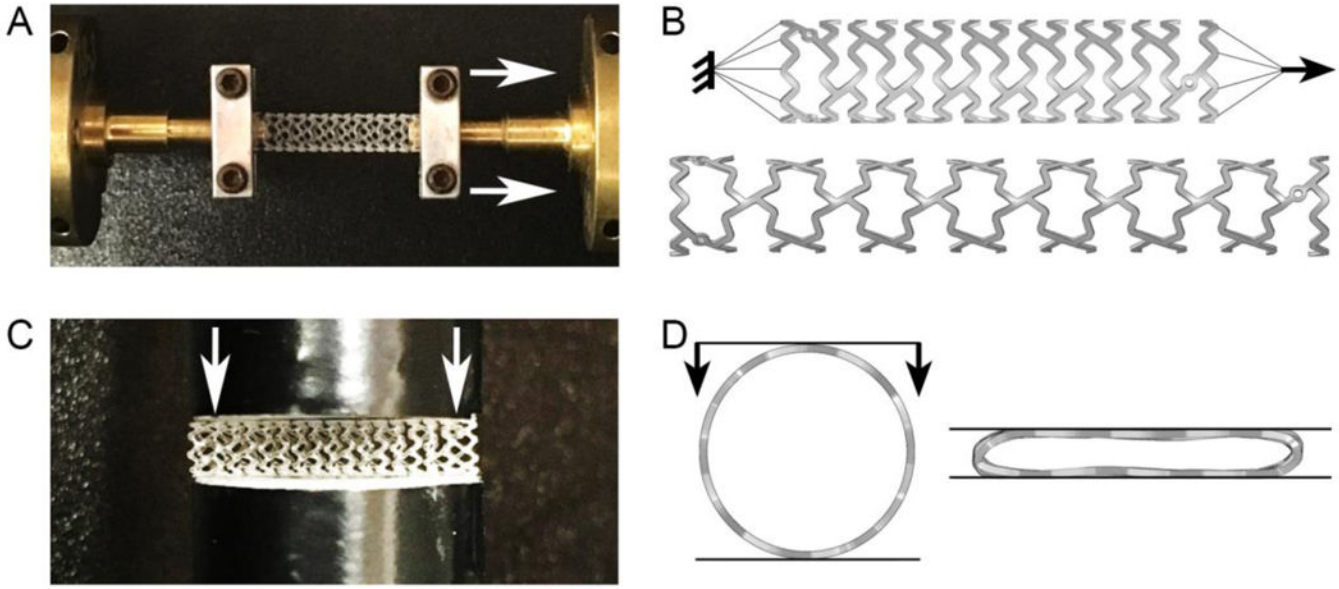

Fig. 3.

Experimental and computational setups for material model validation. (A) Longitudinal tensile test on a full-scale device, (B) the corresponding finite element model of full-scale device before (top) and after (bottom) the longitudinal tensile test, (C) lateral crush resistance test, (D) side view of the corresponding finite element model of full-scale device before (left) and after (right) the lateral crush resistance test.

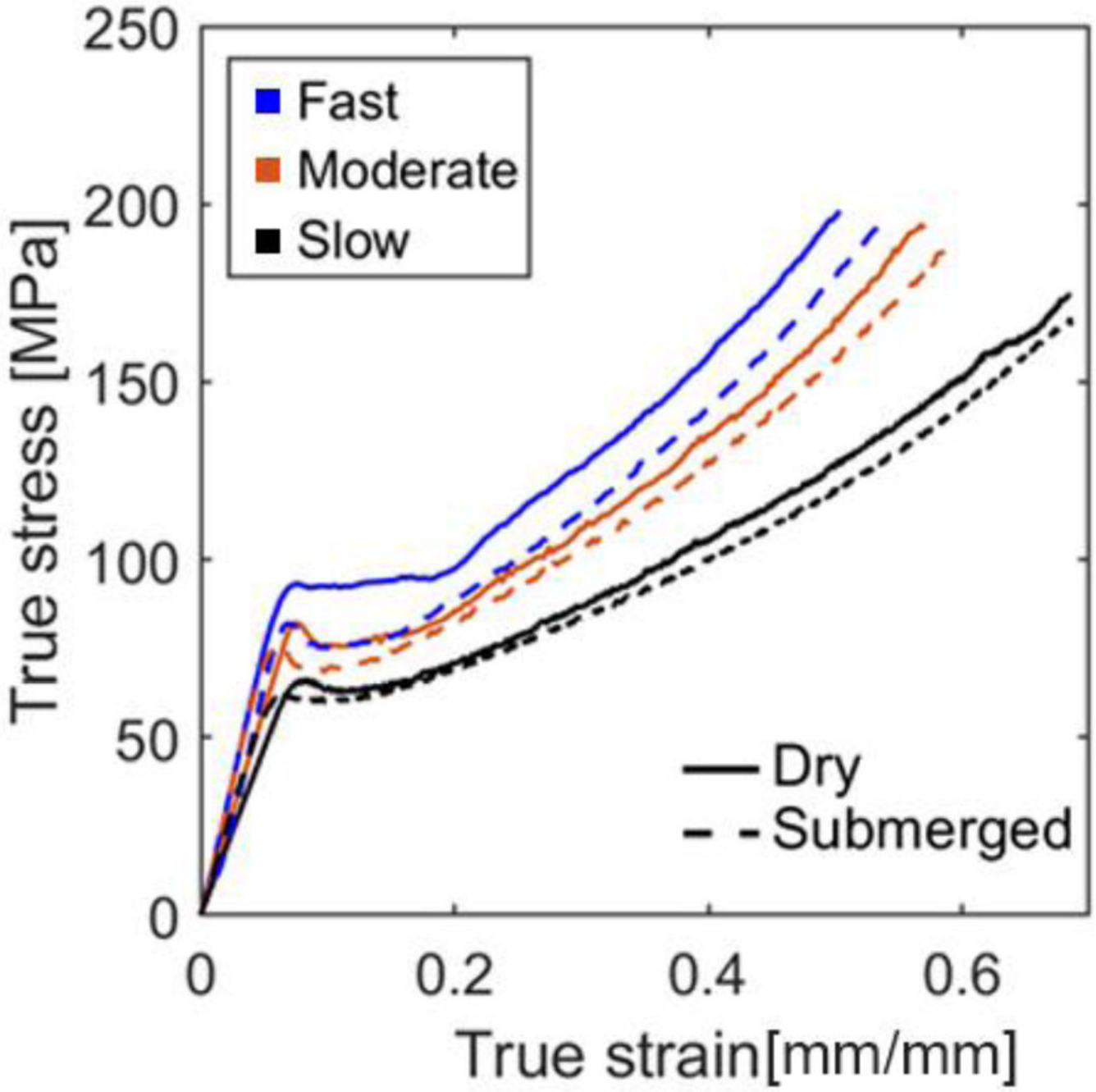

Fig. 4.

True stress–true strain curves of pLLA tested in dry and submerged conditions at different velocities. Fast: 0.1 mm/s, moderate: 0.01 mm/s, and slow: 0.001 mm/s. Only one stress–strain curve is displayed in each testing scenarios for the sake of clarity and to fit all scenarios into one chart for direct comparison. The detailed statistical average and deviation between test methods are presented in Table 3.

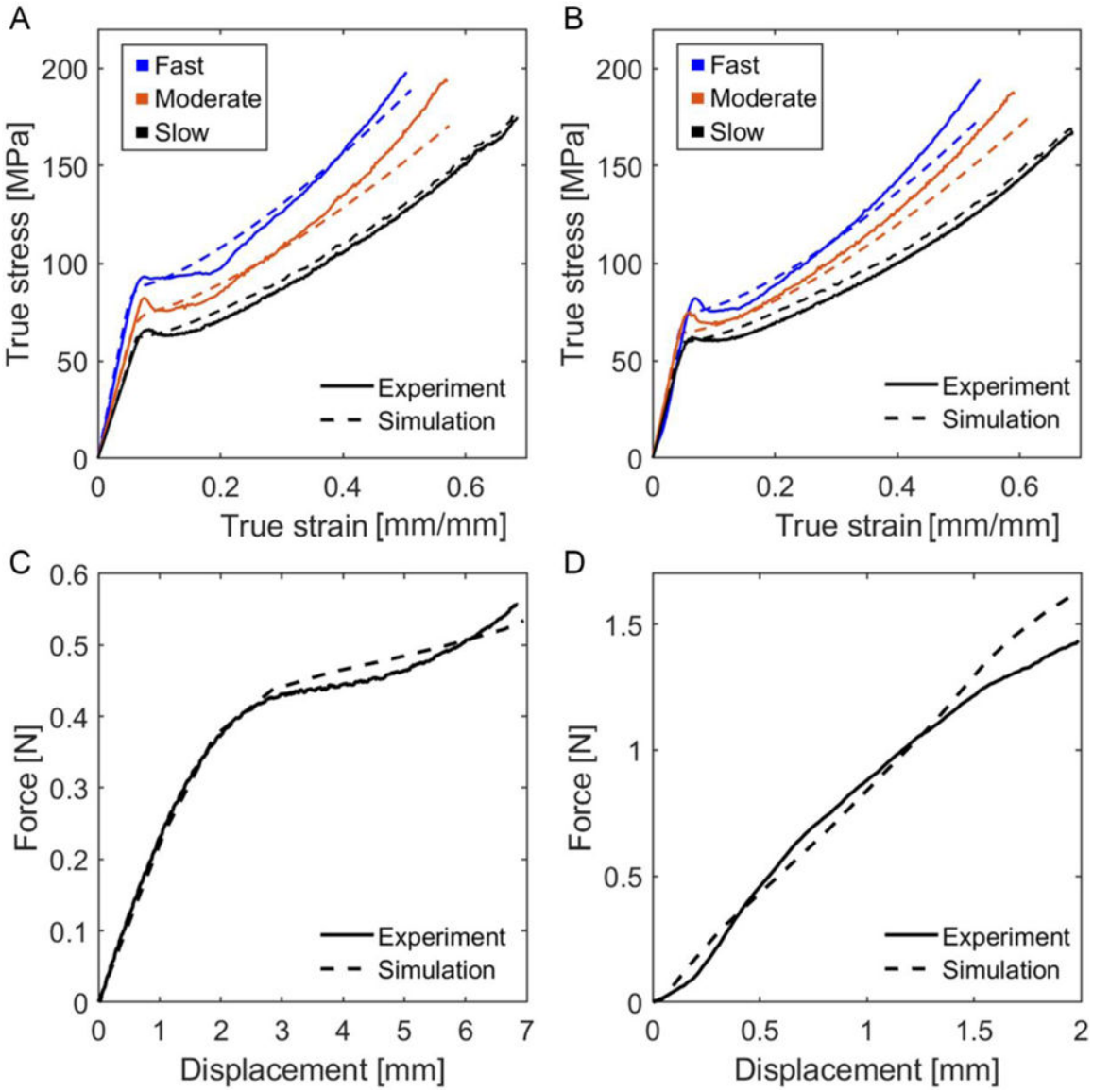

Fig. 5.

Model verification using finite element analysis. Stress–strain curves of dog-bone samples tested at various velocities in (A) dry and (B) submerged conditions. Results of (C) longitudinal tensile and (D) lateral crush resistance test on a full-scale device. Fast: 0.1 mm/s, moderate: 0.01 mm/s, and slow: 0.001 mm/s.

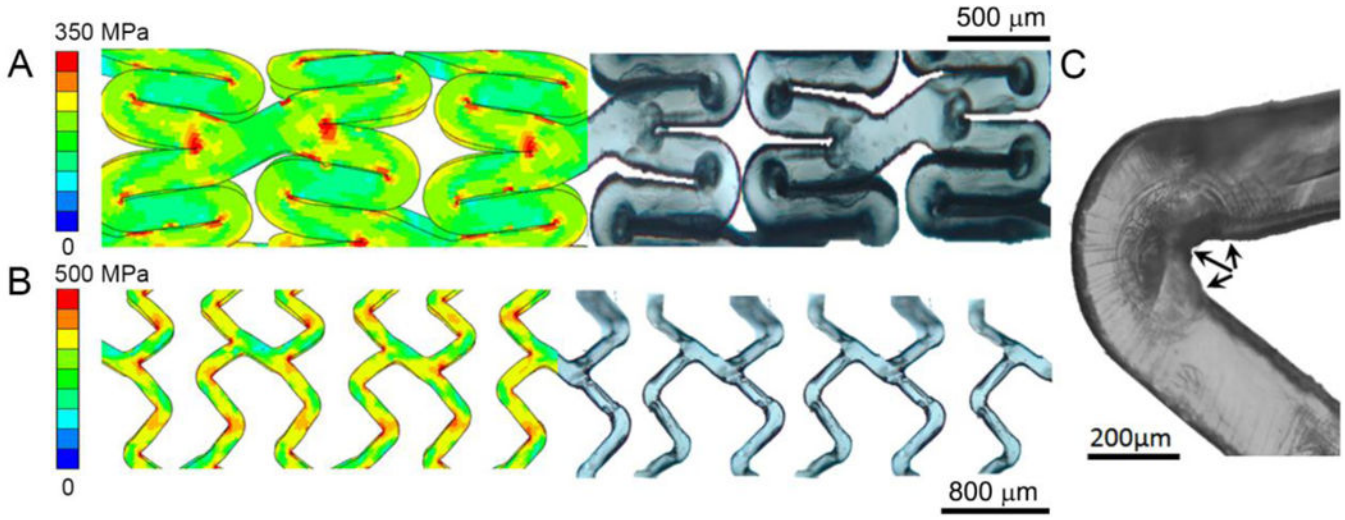

Fig. 6.

Consistency of finite element outputs on von Mises stress concentrated areas and localized damages in microscopic images of (A) crimped and inflated device in a submerged condition at moderate velocity. During crimping, stress concentrated at inner peak edges causes localized deformation. After inflation, deformations observed at outer peak edges. (C) Micro-fractures were found at inner peak edges of a submerged scaffold after inflation at moderate velocity (shown by arrows).

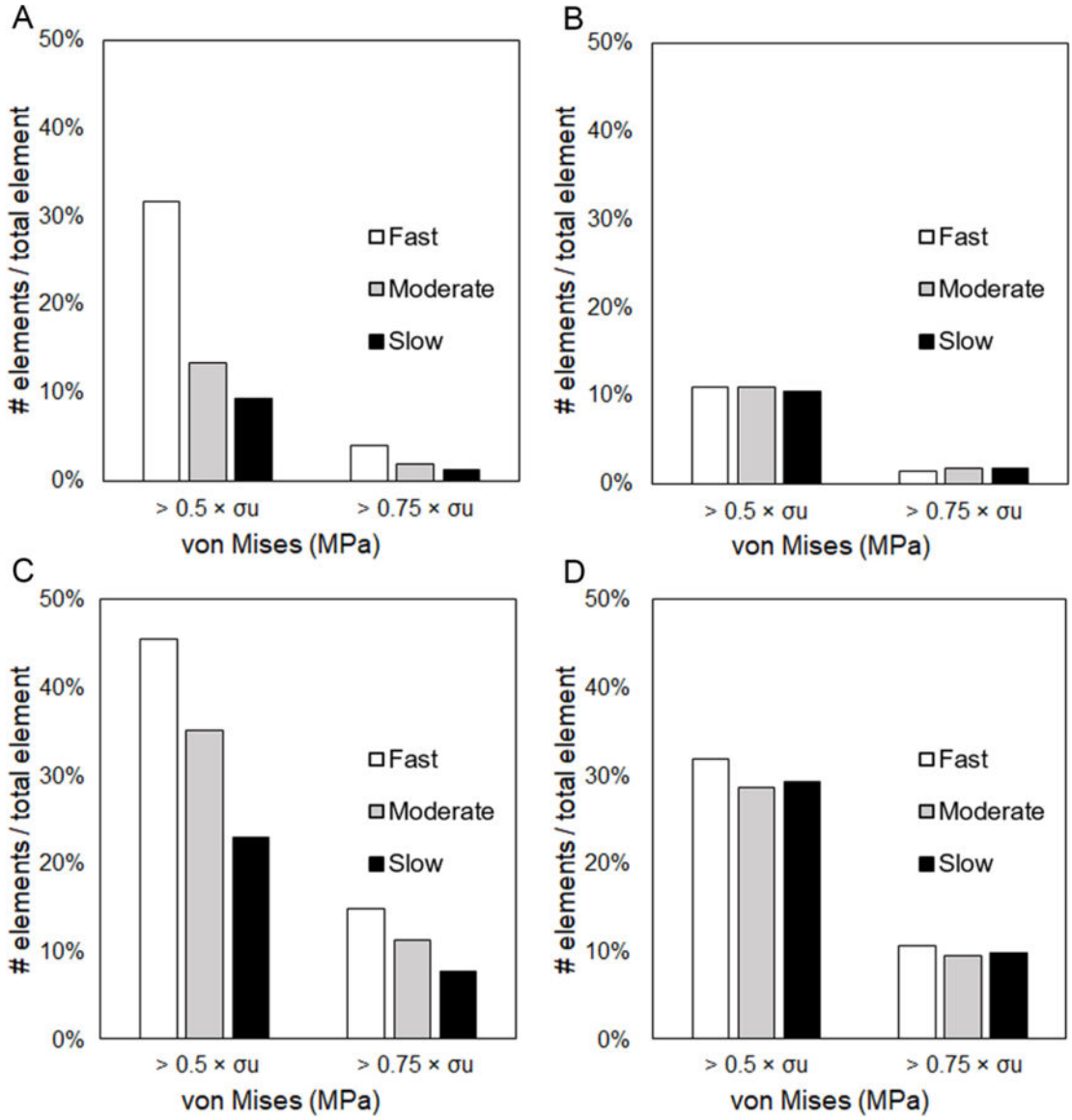

Fig. 7.

Percentage of elements with von Mises stress higher than certain stress thresholds for a device experimented at different procedural rate for crimping at (A) dry and (B) submerged condition, and inflation at (C) dry and (D) submerged condition. The percentage of elements experiencing extreme levels of stresses decrease as the manufacturing/implantation procedure slows down regardless of the functioning environment of the specimen. For submerged samples, at the same rate, less number of elements are exposed to stress extremities.

Table I.

Displacements (U_X) and test duration (ΔT) applied in finite element set-ups to replicate experiments

	Fast (0.1 mm/s)	Moderate (0.01 mm/s)	Slow (0.001 mm/s)
Submerged	U_X=4.18 mm	U_X=5.13 mm	U_X=5.92 mm
	ΔT=46 sec	ΔT=517 sec	ΔT=5960 sec
Dry	U_X=4.00 mm	U_X=4.67 mm	U_X=5.90 mm
	ΔT=43 sec	ΔT=480 sec	ΔT=5950 sec

Table II.

Step duration for step 1 and 4 in each finite element simulation

	Fast	Moderate	Slow
Step 1: Crimping	6 sec	60 sec	600 sec
Step 4: Inflation	10 sec	20 sec	40 sec

Table III:

Key mechanical properties from uniaxial tensile test

	Dry			Submerged		
Testing Velocity (mm/sec)	0.1	0.01	0.001	0.1	0.01	0.001
Elastic Modulus (E, GPa)	1.45 ± 0.113	1.09 ± 0.180	0.94	1.41 ± 0.242	1.44 ± 0.042	1.19
Yield Strain $\left(\bar{\varepsilon}_y\right)$	0.078 ± 0.003	0.079 ± 0.006	0.085	0.068 ± 0.003	0.061 ± 0.001	0.065
Yield Stress $\left(\bar{\sigma}_y\right)$	88.56 ± 3.985	85.46 ± 4.35	65.71	87.00 ± 6.30	71.09 ± 3.29	61.39
Fracture Strain $\left(\bar{\varepsilon}_f\right)$	0.54 ± 0.029	0.57 ± 0.007	0.68	0.55 ± 0.017	0.61 ± 0.021	0.69
Fracture Stress $\left(\bar{\sigma}_f\right)$	195.69 ± 3.16	196.55 ± 3.68	173.77	203.00 ± 9.01	180.09 ± 9.09	166.36

Table IV:

Simulation coefficients. C_1, C_2, C_3, n, and $\dot{\varepsilon}^0$ are material parameters describing the plasticity of the model

	Elastic Modulus (GPa)			Johnson-Cook Plasticity Model				
	0.1 mm/s	0.01 mm/s	0.001 mm/s	C1 (MPa)	C2 (MPa)	C3 (MPa)	n	$\dot{\varepsilon}_0$ (1/s)
Dry	1.5	1.1	0.9	62	223	0.12	1.39	0.0002
Submerged	1.4	1.4	1.2	59	205	0.11	1.40	0.0002